



ARTICLE

3D Gravity Inversion with Correlation Image in Space Domain and Application to the Northern Sinai Peninsula

Xu Zhang¹ Peng Yu² Jian Wang^{3*}

1. Shanghai Shannan Investigation & Design Co.,Ltd. , Shanghai, 201206, China

2. State Key Laboratory of Marine Geology, Tongji University, Shanghai, 200092, China

3. Key Laboratory of Crustal Dynamics, Institute of Crustal Dynamics, China Earthquake Administration, Beijing, 100085, China

ARTICLE INFO

Article history

Received: 15 May 2019

Accepted: 3 June 2019

Published Online: 30 July 2019

Keywords:

3D gravity inversion

Space domain

Correlation image

Effective equivalent storage

Subdomain technique

Northern Sinai Peninsula

ABSTRACT

We present a 3D inversion method to recover density distribution from gravity data in space domain. Our method firstly employs 3D correlation image of the vertical gradient of gravity data as a starting model to generate a higher resolution image for inversion. The 3D density distribution is then obtained by inverting the correlation image of gravity data to fit the observed data based on classical inversion method of the steepest descent method. We also perform the effective equivalent storage and subdomain techniques in the starting model calculation, the forward modeling and the inversion procedures, which allow fast computation in space domain with reducing memory consumption but maintaining accuracy. The efficiency and stability of our method is demonstrated on two sets of synthetic data and one set of the Northern Sinai Peninsula gravity data. The inverted 3D density distributions show that high density bodies beneath Risan Aniza and low density bodies exist to the southeast of Risan Aniza at depths between 1~10 and 20 km, which may be originated from hot anomalies in the lower crust. The results show that our inversion method is useful for 3D quantitative interpretation.

1. Introduction

3D gravity inversion is vital to quantitative interpretation of the Earth's interior compositions and structures. However, gravity inversion is never unique due to the ubiquitous presence of observation errors and the inherent source ambiguity of the gravity potential^[20]. Numerous imaging methods for potential field data have been proposed to estimate source parameters. Patella^[22] presented a probability inversion method which was applied to gravity data by Mauriello and Patella

^[19]. Guo et al.

^[10,20] proposed the correlation image method based on the study of probability images, which produced a higher resolution of density/magnetization distribution by using the vertical gradient of potential data. Fedi^[7,8] presented Depth from Extreme Points (DEXP) method and demonstrated that the resulting image was equivalent to a weighted upward continuation of potential fields by comparing with other methods. Baniamerian et al.^[3,4] proposed a variant of the DEXP method, which generated an image of a quantity proportional to the source distribution. Chauhan et al.^[6] de-

*Corresponding Author:

Jian Wang,

Key Laboratory of Crustal Dynamics, Institute of Crustal Dynamics, China Earthquake Administration, Beijing, 100085, China;

Email: wangjianhyd@163.com

scribed an accurate method for performing upward continuation and vertical differentiation in space domain. Because the methods are all noniterative, stable, and convenient in calculation, they are touted as providing useful starting model for 3D inversion^[8,9].

Forward calculations for potential field are mainly divided into space- and frequency-domains. Space domain methods provide closed-form equations to calculate potential fields directly and accurately. However, when large number of field data is to be modeled, space domain solutions are considerably slow. Frequency domain methods are simpler and faster by using the Fast Fourier Transform, but they have been plagued by imposed periodicity and edge effect (e.g.^[5]).

There are two basic methods to partly overcome the problems of the great cost of computational time and memory footprint in the space domain processing and interpretation: (1) fast calculation of forward modeling, and (2) reducing the number of inversion iterations on the basis of maintaining accuracy. Portniaguine and Zhdanov^[23,29] proposed a compression technique based on cubic interpolation for decreasing computer memory and accelerating the calculation speed. Li and Oldenburg^[16] introduced a wavelet transform to compress the sensitivity matrix and improved the efficiency of forward modeling. Yao^[27] presented an equivalent storage technique based on the equivalence and interchangeability of potential field to inverse gravity and magnetic anomalies for 3D physical properties. Yao et al.^[28] proposed a stochastic subspace technique to reduce the number of inversion dimensions. Shamsipour et al.^[24,25] presented stochastic inversion to reduce the number of inversion iterations. Abedi et al.^[2] applied a bidiagonal matrix with favorable lower dimensions to increase the speed of the algorithm. MohammadRezaie et al.^[18] combined the Krylov method with a regularization method applied to the low-dimensional projected problem.

In this work, we present a 3D gravity inversion with correlation image in space domain. Firstly, we take the 3D correlation image of the vertical gradient of gravity data (CIVG) as a starting model to generate a smooth image. Secondly, we use effective equivalent storage and subdomain techniques to increase the computational speed of forward modeling. Thirdly, 3D density distributions are obtained by inverting CIVG to fit the synthetic/field data using the steepest descent method. Because the effective equivalent storage and subdomain techniques are utilized to the starting model calculation of the forward modeling and the inversion, all these processes can be carried out fast in space domain with reducing memory consumption but maintaining accuracy. We further verify the feasibility and stability of the method by applying on the field data of the

Northern Sinai Peninsula.

2. Methodology

2.1 Gravity Data and Its Vertical Gradient Correlation Image

Guo et al.^[10] presented a correlation image method for gravity data and its vertical gradient on regular gridded data. Suppose that the z-axis is positive downwards, and the observation plane is at zero level. The gravity anomaly caused by an arbitrary cell q with volume V can be expressed as

$$g(x_i, y_i) = GV\Delta\sigma_q B_q(x_i, y_i), \text{ *MERGEFORMAT (1)}$$

where G is the Newton's gravitational constant, $\Delta\sigma_q$ is the density contrast between the anomalous body and background mass, and $B_q(x_i, y_i)$ is a geometrical function

$$B_q(x_i, y_i) = \frac{z_q}{r(x_i, y_i)^3}, \text{ *MERGEFORMAT (2)}$$

here $r(x_i, y_i) = [(x_q - x_i)^2 + (y_q - y_i)^2 + z_q^2]^{1/2}$, (x_i, y_i) is the observation point at sea level, and (x_q, y_q, z_q) is the source point.

The normalized correlation between the observed and forward data is calculated as follow^[10]

$$C_q(x_q, y_q, z_q) = \frac{\sum_{i=1}^N \Delta g(x_i, y_i) \Delta g_q(x_i, y_i)}{\sqrt{\sum_{i=1}^N \Delta g^2(x_i, y_i) \sum_{i=1}^N \Delta g_q^2(x_i, y_i)}}, \text{ *MERGEFORMAT (3)}$$

where $\Delta g(x_i, y_i)$ is the observation data, $C_q(x_q, y_q, z_q)$ is the coefficient of normalized correlation, and N is the total number of observation points. If $\Delta\sigma_q$ is positive, Eq. (3) can be simplified to

$$C_q(x_q, y_q, z_q) = \frac{\sum_{i=1}^N \Delta g(x_i, y_i) B_q(x_i, y_i)}{\sqrt{\sum_{i=1}^N \Delta g^2(x_i, y_i) \sum_{i=1}^N B_q^2(x_i, y_i)}}, \text{ *MERGEFORMAT (4)}$$

and according to the Cauchy inequality, we can obtain

$$-1 \leq C_q(x_q, y_q, z_q) \leq 1. \text{ *MERGEFORMAT (5)}$$

CIVG can also be expressed in the same way

$$C_{q,z}(x_q, y_q, z_q) = \frac{\sum_{i=1}^N \Delta g_z(x_i, y_i) B_{q,z}(x_i, y_i)}{\sqrt{\sum_{i=1}^N \Delta g_z^2(x_i, y_i) \sum_{i=1}^N B_{q,z}^2(x_i, y_i)}}, \quad \backslash*\text{MERGEFORMAT (6)}$$

in which $\Delta g_z(x_i, y_i)$ is the vertical gradient of the observation data, and $B_{q,z}(x_i, y_i)$ is the vertical gradient of $B_q(x_i, y_i)$, which is also a geometrical function

$$B_{q,z}(x_i, y_i) = \frac{2z_q^2 - (x_q - x_i)^2 - (y_q - y_i)^2}{\left[(x_q - x_i)^2 + (y_q - y_i)^2 + z_q^2 \right]^{5/2}} = \frac{3z_q^2 - r^2}{r^{5/2}}. \quad \backslash*\text{MERGEFORMAT (7)}$$

The correlation image of either the gravity anomaly or the vertical gradient is equivalent to a weighted upward continuation reflecting the density distribution characteristics. Therefore, CIVG is considered as a useful starting model for the subsequent 3D inversion, which can reduce non-uniqueness, uncertainty and the number of iterations.

2.2 Equivalent Storage Technique

Yao^[27] proposed an equivalent storage technique based on the equivalence of shift and the symmetry reciprocation of potential field (Figure 1). From Eq. (2), we can see that the geometrical function is only determined by the distances from the centers of cells to the observation points, when the sources locating within one layer. Take the first layer as an example, the distance from the first grid of this layer to the first observation point is equal to the distance from an arbitrary grid of the layer to its corresponding observation point (Figure 1a), which can be written as^[27]

$$B_{(1,1)}(1,1) = B_{(1,2)}(1,2) = \dots = B_{(i,j)}(i,j) = \dots = B_{(m,n)}(m,n), \quad \backslash*\text{MERGEFORMAT (8)}$$

here $B_{(i,j)}(i,j)$ is the geometrical function of Eq. (2), the subscript $(i,j,1)$ is the source points, (i,j) is the observation point at sea level, and (m,n) is the size along the X - and Y -directions. According to the plane geometry theory, the segments sandwiched between two parallel planes are equals, and then Eq. (8) can be extended to

$$B_{(1,1)}(k,l) = \dots = B_{(i,j)}(i+k-1, j+l-1) = \dots = B_{(m-k+1, n-l+1)}(m,n). \quad \backslash*\text{MERGEFORMAT (9)}$$

Based on Eq. (9), the geometrical function of an arbitrary point can be replaced by the first point on the same

layer. The interchangeability of the geometrical functions can be written as

$$B_{(1,1)}(k,l) = B_{(k,l)}(1,1) = \dots = B_{(i+k-1, j+l-1)}(i,j) = B_{(i,j)}(i+k-1, j+l-1), \quad \backslash*\text{MERGEFORMAT (10)}$$

combining Eq. (9) with Eq. (10), we obtain

$$B_{(i,j)}(k,l) = B_{(1,1)}(|i-k|+1, |j-l|+1). \quad \backslash*\text{MERGEFORMAT (11)}$$

Figure 1 is the sketch map showing the distances between the sources and observation points used for equivalent storage technique. When grid meshing has been suitably established, the geometry of gridding is fixed in the iterative inversion. We can then employ the equivalent storage technique to relax the demand on computer memory and increase the computational efficiency. It is worth mentioning that the technique works when the gridding of 3D domain along the X - and Y -directions is the same as that used for the observation plane.

2.3 Subdomain Technique

To further increase the computational speed and reduce the memory usage, we propose a technique of subdomain in this section. We calculated the gravity anomaly by an infinitely extended line along the X -axis with depth z_q from gridded data. We assume a line segment length a with density σ , the outline length $2(b-a)$ with density $k\sigma$, here b is infinity, and k is constant. The gravity anomaly above the center of line segment can be expressed as

$$\begin{aligned} \Delta g &= G\sigma v_q \int_{-a}^a \frac{z_q}{r(x_i, y_i)^3} dx = G\sigma v_q \int_{-a}^a \frac{z_q}{\left((x_q - x_i)^2 + z_q^2 \right)^{3/2}} dx \\ &= G\sigma v_q \left[\frac{a}{z_q \sqrt{a^2 + z_q^2}} - \left(\frac{-a}{z_q \sqrt{a^2 + z_q^2}} \right) \right] = G\sigma v_q \frac{2a}{z_q \sqrt{a^2 + z_q^2}}. \end{aligned} \quad \backslash*\text{MERGEFORMAT (12)}$$

Then the ratio of the gravity anomalies between the whole line and the line segment can be expressed as

$$\begin{aligned} \frac{\Delta g_2}{\Delta g_1} &= \frac{Gk\sigma v_q \frac{2(b-a)}{z_q \sqrt{b^2 + z_q^2}} - G\sigma v_q \frac{2a}{z_q \sqrt{a^2 + z_q^2}}}{G\sigma v_q \frac{2a}{z_q \sqrt{a^2 + z_q^2}}} \\ &= \frac{Gk\sigma v_q \frac{2b}{z_q \sqrt{b^2 + z_q^2}} - G(k-1)\sigma v_q \frac{2a}{z_q \sqrt{a^2 + z_q^2}}}{G\sigma v_q \frac{2a}{z_q \sqrt{a^2 + z_q^2}}} \\ &= \frac{k \left(\frac{2b}{z_q \sqrt{b^2 + z_q^2}} - \frac{2a}{z_q \sqrt{a^2 + z_q^2}} \right)}{\frac{2a}{z_q \sqrt{a^2 + z_q^2}}} + 1 = k \frac{b\sqrt{a^2 + z_q^2} - a\sqrt{b^2 + z_q^2}}{a\sqrt{b^2 + z_q^2}} + 1, \end{aligned} \quad \backslash*\text{MERGEFORMAT (13)}$$

Because b is infinity number, we can obtain

$$\frac{\Delta g_2}{\Delta g_1} = k \frac{b\sqrt{a^2 + z_q^2} - ab}{ab} + 1 = k \left(\sqrt{1 + \left(\frac{z_q}{a}\right)^2} - 1 \right) + 1,$$

*MERGEFORMAT (14)

assuming $a = 20z_q$, and $k = 10$, then

$$\frac{\Delta g_2}{\Delta g_1} = 10 \left(\sqrt{1 + \left(\frac{1}{20}\right)^2} - 1 \right) + 1 = 10 \times 0.001 + 1 = 1.01$$

*MERGEFORMAT (15)

Eq. (15) implies that the subdomain technique is an approximate quantitative determination method to reduce the computational time of forward modeling with a high fitting accuracy. Due to the line is arbitrary, and all other lines can be applied in the same layer, this technique can be extended to the entire plane.

Here we take an example to illustrate the efficiency of the combined techniques of equivalent storage and subdomain. A 3D domain is divided into $1000 \times 1000 \times 10$ cubic prisms with a grid spacing of 1, and the observation data are also calculated on a 1000×1000 grid with an interval of 1. The storage of a geometrical function is 10^{13} without using the equivalent storage technique, whereas the storage is 10^7 if using the equivalent storage technique. With the subdomain technique, the storage can be further reduced to be 10^5 .

2.4 The Steepest Descent Inversion Method

The conventional way of solving ill-posed inverse problems is based on the misfit functional determined as a norm of difference between the observed and theoretical data

$$p(m, d) = \|A(m) - d\|^2 = \min, \text{ *MERGEFORMAT (16)}$$

where, A is the forward modeling operator, d is the observation data.

In this study, we apply the steepest descent method to inverse the 3D density distribution. One iteration step, from iteration number n to number $n+1$, can be summarized as follows^[30]

$$\begin{aligned} r_n &= A(m_n) - d \\ I_n &= A^T r_n \\ s_n &= AI_n \\ k_n &= \|s_n\|^2 / \|I_n\|^2 \\ m_{n+1} &= m_n - k_n I_n, \text{ *MERGEFORMAT (17)} \end{aligned}$$

where I_n is the steepest descent direction, k_n is the step length in the direction, r_n is the residual between the observed and theoretical data.

2.5 Inversion Strategy

The following is a summary of the inversion strategy we used to apply correlation image theory and effective equivalent storage and subdomain techniques to obtain 3D density distribution (Figure 2):

(1) we calculate the geometrical function of the point located in the first row and the first column of the 3D domain using Eqs. (2) and (7);

(2) we calculate CIVG as a starting model using Eq. (6) with the effective equivalent storage (Eq. (11)) and subdomain techniques (Eq. (14)) for fast computation;

(3) we use the steepest descent method for iteration inversion, containing the effective equivalent storage and subdomain techniques for increasing the computation speed;

(4) the final 3D density distribution is obtained after achieving the minimum error or the number of iterations by the steepest descent inversion method;

(5) output the results.

3. Synthetic Model Test

In this section, we apply our fast inversion strategy on two sets of synthetic data: 1) a prism model, and 2) an interface model. The computational time and root-mean-square error (RMSE) of each modeling and inversion are calculated by a personal computer with 4 GB RAM, 3.10 GHz processor on a 32-bit operating system. No priori geologic information has been used to constrain the inversions for either of the two data sets. Therefore, the density variance is from zero to infinity.

The first model (Model 1) consists of two close prismatic sources (solid lines) with same size. They are buried at a depth of 5 km with a density contrast of 0.1 g/cm^3 . The 3D domain is divided into $50 \times 50 \times 20$ cubic prisms with a grid spacing of 1 km. We add pseudo-random Gaussian noise to the synthetic data with mean value of zero and standard deviation of 0.03 mGal. The gravity anomaly is calculated on a $50 \times 50 \text{ km}^2$ grid with a grid spacing of 1 km along the x - and y -directions (Figure 3a).

Figure 3b shows the anomaly calculated by taking a semi-infinite model with density contrast of 0 g/cm^3 . This is usually used as starting values of density in the inversion when there is no prior information available. Figure 3d and g shows the estimated density distribution after 10 iterations at slices of $z = 1 \text{ km}$ and $y = 25 \text{ km}$,

respectively. The calculated gravity perfectly matches the observed values with an RMSE of 0.12. The density distributions are mainly concentrated in a shallow subsurface with very small density values. Figure 3c shows the estimated anomaly using our inversion strategy by taking CIVG as a starting model, while Figure 3e and h shows the density distribution of the starting model, and Figure 3f and i show the inverted results after 15 iterations at slices of $z = 1$ km and $y = 25$ km, respectively. It can be seen that the CIVG produces smooth models (Figure 3e and h). The final density distribution generates a clear, sharp, high-quality image, and the density value is close to the actual value (Figure 3f and i).

To further evaluate the computational efficiency of our inversion strategy, we use a more complex basement interface model (Model 2) with a density contrast of 0.2 g/cm^3 (Figure 4). The 3D domain is divided into $150 \times 30 \times 10$ cubic prisms with a grid spacing of 1 km along the x -, y - and z -directions. Figure 4a presents the synthetic gravity anomaly and Figure 4b shows the starting model using CIVG at slice of $y = 15$ km. Figure 4c and d shows the estimated anomaly and the inverted result at slice of $y = 15$ km without the subdomain technique. Figure 4e and f shows the estimated anomaly and the inverted result with subdomain technique. The observation anomaly can be fitted using the proposed procedure in this study with or without subdomain technique from comparing Figure 4c and e with Figure 4a. Meanwhile, comparing with Figure 4b, the result of our method (Figure 4d and f) clearly outlines the fluctuation of the interface and enhances the visibility and sharpness of geological structures, and is close to the true interface.

Table 1 shows the statistical information of the two different synthetic models. Form Model 1, although the semi-infinite model can reconstruct the anomaly with fewer iterations, less time than CIVG, the density distribution is quite deviate from the true position and the numerical value is smaller than the actual value. It is worth noting that the small RMSE and good fitting of anomaly do not represent the real underground density distribution, which is the manifestation of multi-solution inversion. Therefore, CIVG is a better choice as a starting model without prior information. Form Model 2, Subdomain technique takes less time and has smaller RMSE with the same number of iterations, comparing between Figure 4d and f. Subdomain technique greatly improves computational efficiency without losing accuracy, the larger the data set, the more efficient our method. It should be pointed out that we can reduce the grid spacing to achieve higher resolution results with the time and memory decreasing by our method.

4. 3D Gravity Inversion of the Northern Sinai Peninsula

In this section, we further apply our 3D inversion method to obtain density distributions of the Northern Sinai Peninsula and compare our density results with previous study^[11]. The Sinai Peninsula is located between the Mediterranean and Red seas and is bounded by the Gulf of Suez to the west and the Dead Sea Transform to the east (Figure 5). The study area is a continental block between the African and Arabian plates, and underwent complex tectonics due to the interactions of different tectonic units. During the Late Triassic, the breakup of the north Afro-Arabian plate and the opening of the Tethys reactivated ENE-WSW trending deep faults. As the African plate moved towards to the Eurasian plate, the Tethys Sea began to close during the Late Cretaceous to pre-Miocene times, resulting in a series of NE-ENE oriented doubly plunging folds originated from inversion of the Mesozoic extensional basins in the Northern Sinai Peninsula. These inversion folds connected with the Syrian Arc Fold Belt to the northeast^[12,21]. The aim of the present study is to carry out 3D gravity inversion to obtain density distribution of the Northern Sinai Peninsula and to help further understand the major tectonic and geologic characteristics.

The Bouguer gravity anomaly is reproduced in Figure 5a after digitizing the anomaly presented by Khalil et al.^[11]. A gravity high is observed at Risan Aniza to the south of EI-Arish, and it decreases gradually to a medium value at Sheikh Zwayed, whereas gravity lows are observed to the southeast of Risan Aniza. Figure 6b shows the residual anomalies based on the method of Abdelrahman et al.^[11]. Both Risan Aniza and Sheikh Zwayed show high positive values on the residual Bouguer anomaly map, indicating high density bodies underneath these regions. Southeast of Risan Aniza, large area exhibits negative anomalies, implying low densities at depth. In this study, we utilize the inversion strategy proposed in section 2.5 to obtain the 3D density distributions from the residual Bouguer anomalies (Figure 6b).

The inversion domain is divided into $101 \times 113 \times 10$ cubic prisms with a grid spacing of 1 km along the x -, y - and z -directions. The background density value is taken as 2.67 g/cm^3 , and the minimum and maximum density values are assumed to be 2.2 g/cm^3 and 2.9 g/cm^3 according to the known geological and geophysical investigations of the study area, respectively. Therefore, the density contrast ranges from -0.47 to 0.23 g/cm^3 across the study area.

Figure 7 shows the initial density distributions, which are calculated by the linear superposition of relative densities (calculated from correlation images based on Eq. (6)) and the background density (2.67g/cm^3) at different depths (1, 2, 3, 5, 10 and 20 km). Figure 7a shows the estimated gravity anomaly after 12 iterations, and the computational time and RMSE are 21 s and 0.19, respectively. The fitting errors, which are the differences between the residual and estimated data, are shown in Figure 8b.

Figure 9 shows the final density distributions at the corresponding depths. Although the final density maps are very similar with the initial density images (Figure 7), there are big differences in the values of density. Our final density distribution model shows distinct high values beneath Risan Aniza at all depth slices (Figure 9). High density bodies are also observed under Sheikh Zwayed at depths between 3 and 20 km. It is interesting that the region to the southeast of Risan Aniza exhibits a slight high density anomaly below 5 km and an evident low density anomaly between 10 and 20 km. Li et al. [13] presented relatively small Curie depths in the same region, indicating a thermal anomaly at depth, therefore resulting in low density bodies to the southeast of Risan Aniza. Based on the horizontal slices, we suggest that there are two deep regional NE-SW trending faults around the high-density contrasts in the northern and southern edges of the Risan Aniza fold zone. We also build a density profile AA1 across EI Arish and Risan Aniza (Figure 9g), which shows medium and high density bodies beneath these two regions, respectively. To the southeast of Risan Aniza, the density distribution changes distinctly from low to high anomalies at depth, which may be caused by hot materials in the lower crust.

5. Conclusions

In this paper, we present a 3D gravity inversion method based on correlation image to recover density distributions in space domain. Our method applies CIVG as a starting model to generate a higher resolution image. In addition to the effective equivalent storage, we propose the subdomain techniques for fast calculation of the forward modeling and correlation image, which can reduce the consumption of memory without losing accuracy. We verify the feasibility and stability of our method by testing on both the synthetic and field data. High densities are observed beneath Risan Aniza, whereas low densities exist to the southeast of Risan Aniza at depths between 10 and 20 km, which may be resulted from hot anomalies in the lower crust.

Acknowledgements

We would like to thank the Editor Professor Sayed Hemeda and an anonymous reviewer for their insightful and constructive reviews and comments. This research is funded by the Institute of Crustal Dynamics, China Earthquake Administration (Grant No. ZDJ2019-09), the National Science Foundation of China (Grant No. 41704086), and the National Key Research & Development Program (2016YFC060110401).

Supplements

Table 1. Statistical information of two different synthetic models

Model	Starting model	Subdomain technique	Iterations	RMSE	Computation time(s)
Model 1	Semi-infinite	NO	10	0.12	22
Model 1	CIVG*	NO	15	0.12	44
Model 2	CIVG	NO	16	0.45	63
Model 2	CIVG	YES	16	0.32	46

Note: *CIVG is 3D correlation image of the vertical gradient of gravity data.

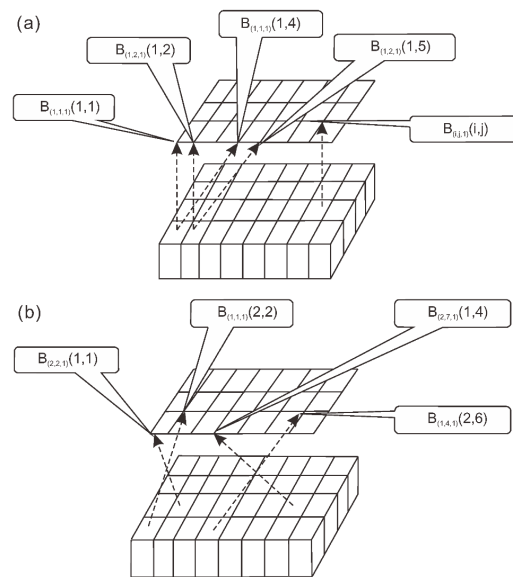


Figure 1. Illustration of the equivalent storage technique

Note: (a) equivalence of shift, and (b) symmetry reciprocity. $B_{(i,j,1)}(i,j)$ is the geometrical function of Eq. (2), the subscript $(i,j,1)$ is the source point, and (i,j) is the observation point at sea level.

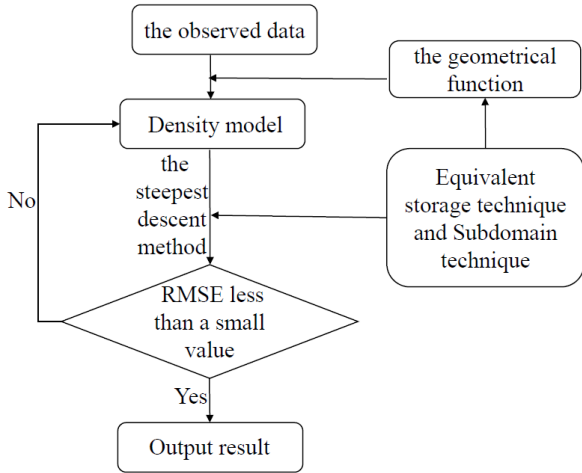


Figure 2. Flow chart of 3D gravity inversion with CIVG in space domain

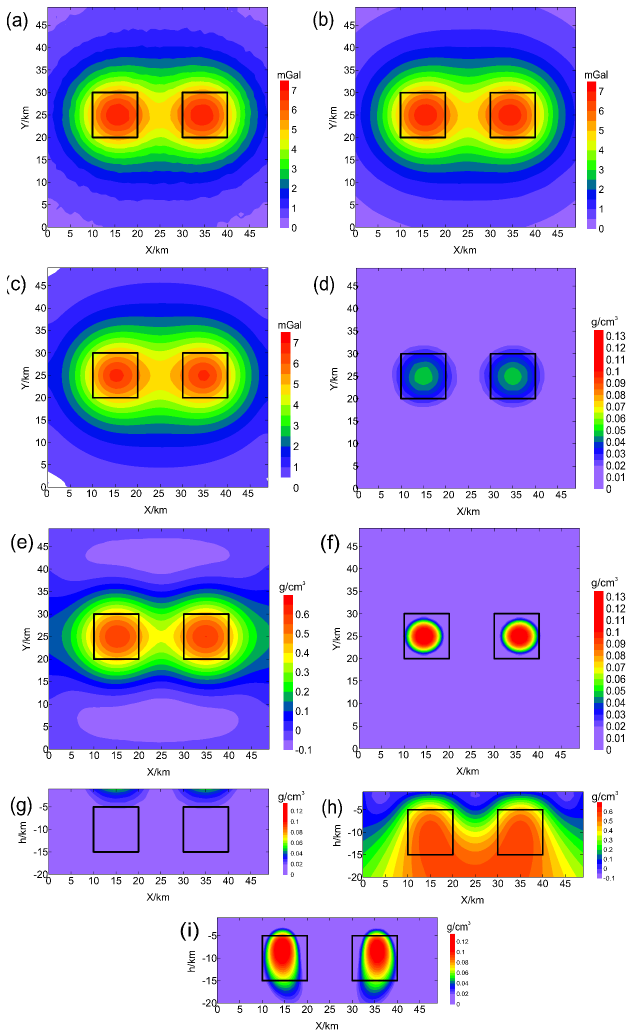


Figure 3. Synthetic tests on the prism model

Note: (a) theoretical gravity anomaly, (b) gravity anomaly calculated by taking the density contrast as 0 g/cm^3 based on a semi-infinite model, (c)

estimated gravity anomaly based on our inversion strategy with CIVG, (d) estimated density distribution from the semi-infinite model with density contrast of 0 g/cm^3 at slice of $z=1 \text{ km}$, (e) density distribution of starting model at slice of $z=10 \text{ km}$, (f) inverted result at slice of $z=10 \text{ km}$, (g) estimated density distribution from the semi-infinite model at slice of $y=25 \text{ km}$, (h) density distribution of the starting model at slice of $y=25 \text{ km}$, and (i) inverted result at slice of $y=25 \text{ km}$. The black lines are the boundaries of the synthetic models.

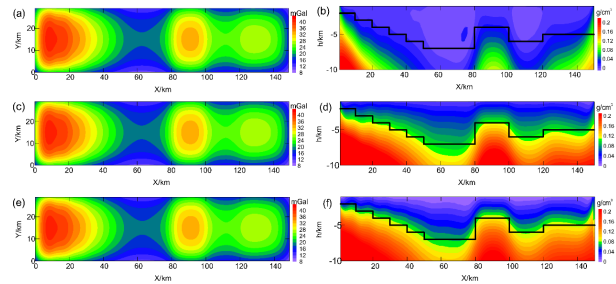


Figure 4. Synthetic tests on the interface model

Note: (a) theoretical gravity anomaly, (b) the starting model using CIVG at slice of $y=15 \text{ km}$, (c) estimated gravity anomaly without subdomain technique, (d) inverted result without subdomain technique at slice of $y=15 \text{ km}$, (e) estimated gravity anomaly with subdomain technique, and (f) inverted result with subdomain technique at slice of $y=15 \text{ km}$. The black lines are the boundaries of the synthetic models.

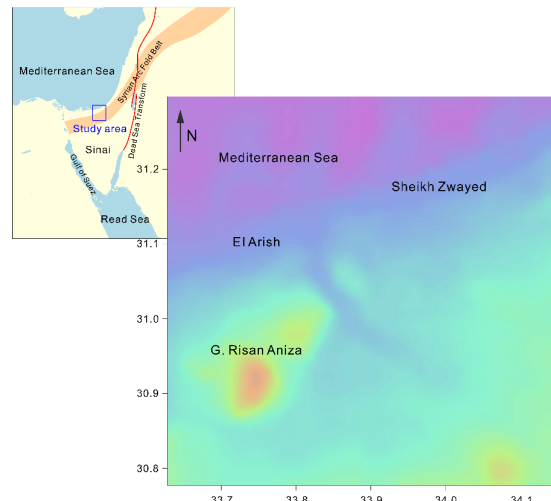


Figure 5. Topographic map of the study area. The inset shows the regional tectonic map of the Sinai and the neighboring area

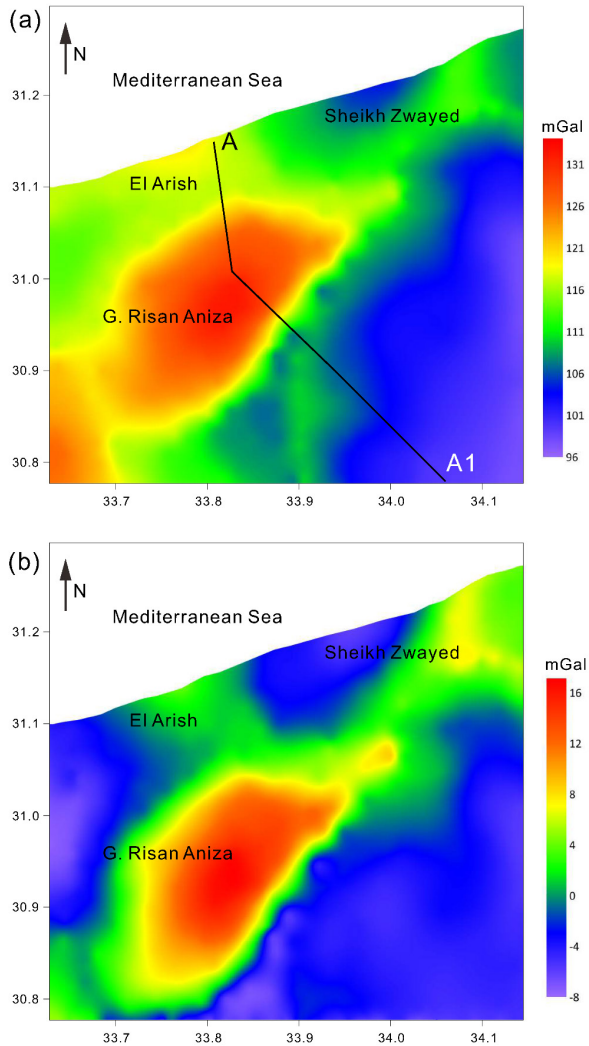


Figure 6. (a) Digitized Bouguer gravity anomaly of the Northern Sinai Peninsula^[11]. The black line is the location of density profile AA1 for Figure 9g. (b) Residual Bouguer gravity anomaly of the Northern Sinai Peninsula

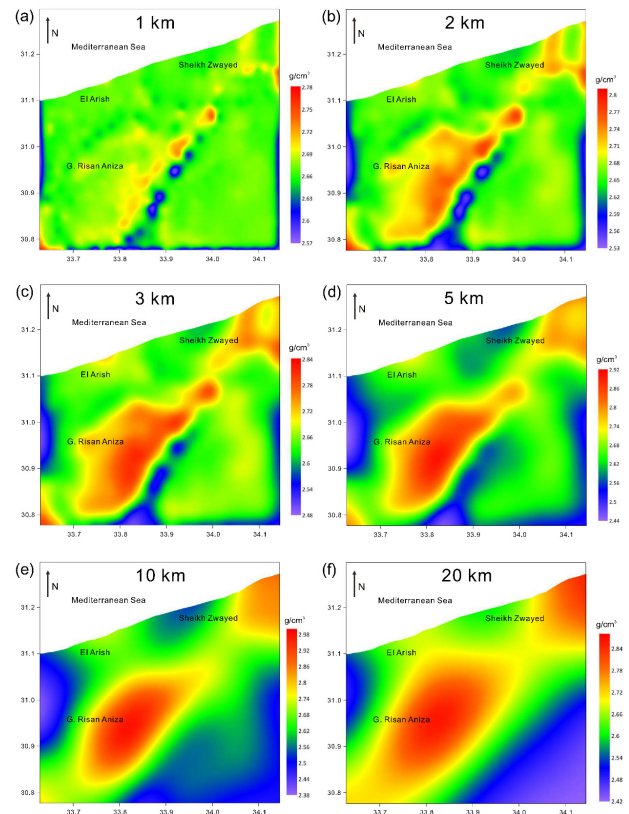


Figure 7. Initial density models at different depths of (a) 1 km, (b) 2 km, (c) 3 km, (d) 5 km, (e) 10 km and (f) 20 km

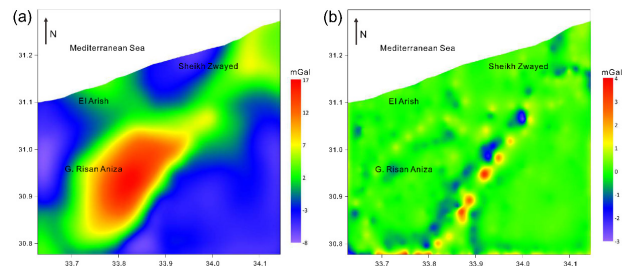


Figure 8. (a) Estimated gravity anomaly after 12 iterations and (b) differences between the residual and estimated gravity data

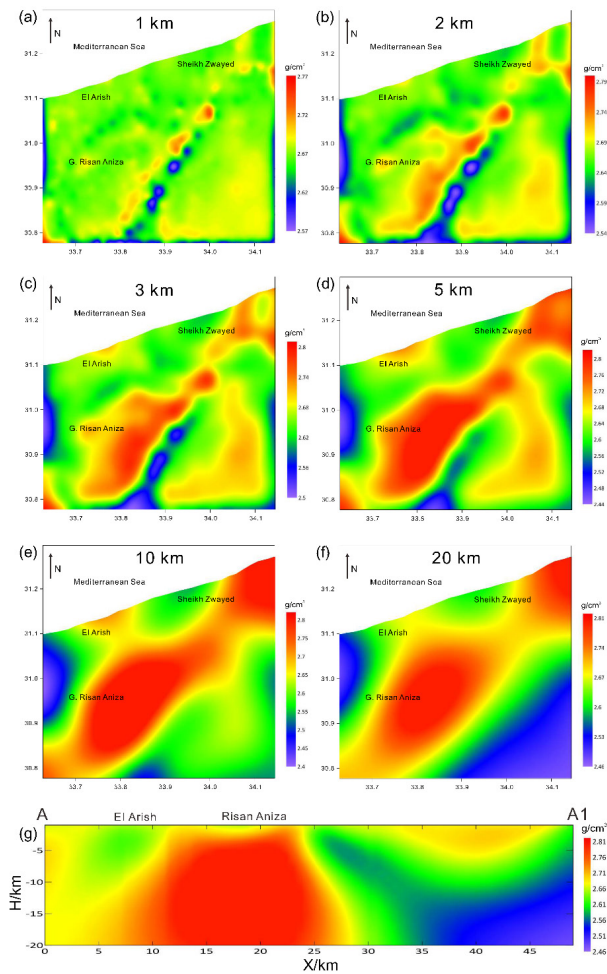


Figure 9. Estimated density distributions at different depths of (a) 1 km, (b) 2 km, (c) 3 km, (d) 5 km and (e) 10 km and (f) 20 km, and (g) is the density distribution profile AA1 according to Figure 6a

References

[1] Abdelrahman, E.M., Radwan, A.H., Issawy, E.A., El-Araby, H.M., El-Araby, T.M., Abo-Ezz, E.R.. Gravity interpretation of vertical faults using correlation factors between successive least-squares residual anomalies. *Mining Pribram Symp. on Mathematical Methods in Geology*, 1999, MC2: 1-6.

[2] Abedi, M., Gholami, A., Norouzi, G.H., Fathianpour, N.. Fast inversion of magnetic data using Lanczos bidiagonalization method. *Journal of Applied Geophysics*, 2013, 90: 126-137.

[3] Baniamerian J., Oskooi B. and Fedi M.. source imaging of potential fields through a matrix space-domain algorithm, *Journal of Applied Geophysics*, 2017, 136: 51.

[4] Baniamerian J., Fedi M. and Oskooi B.. Compact Depth from Extreme Points: a tool for fast potential

field imaging. *Geophysical prospecting*, 2016, 64: 1386-1398.

[5] Charles F. Van Loan.. *Computational Frameworks for the Fast Fourier Transform*, 1992.

[6] Chauhan M.S., Fedi M. and Mrinal K. S.. Gravity inversion by the Multi-Homogeneity Depth Estimation method for investigating salt domes and complex sources, *Geophysical Prospecting*, 2018, 66: 175-191.

[7] Fedi M.. "DEXP: A fast method to determine the depth and the structural index of potential fields sources." *Geophysics*, 2007, 72(1): I1-I11.

[8] Fedi M. and Pilkington M.. "Understanding imaging methods for potential field data." *Geophysics*, 2012, 77(1): G13-G24.

[9] Gibert D. and Sailhac P.. Comment on: self-potential signals associated with preferential groundwater flow pathways in sinkholes. *Journal of Geophysical Research*, 2008, 113.

[10] Guo, L.H., Meng, X.H., Shi, L.. 3D correlation imaging of the vertical gradient of gravity data. *J Geophys Eng*, 2011, 8: 6-12.

[11] Khalil, M.A., Santos, F.M.. 3D Gravity Inversion of Northern Sinai Peninsula: A Case Study. *Pure Appl Geophys*, 2014, 171: 1557-1569.

[12] Khalil, M.A., Santos, F.M., Farzamian, M.. 3D gravity inversion and Euler deconvolution to delineate the hydro-tectonic regime in El-Arish area, northern Sinai Peninsula. *Journal of Applied Geophysics*, 2014, 103: 104-113.

[13] Li, C.-F., Lu, Y. and Wang, J.. A global reference model of Curie-point depths based on EMAG2. *Scientific Reports*, 2017, 7: 45129.

[14] Li, Y., Oldenburg, D.W.. 3-D inversion of magnetic data. *Geophysics*, 1996, 61: 394-408.

[15] Li, Y., Oldenburg, D.W.. 3-D inversion of gravity data. *Geophysics*, 1998, 63: 109-119.

[16] Li, Y.G., Oldenburg, D.W.. Fast inversion of large-scale magnetic data using wavelet transforms and a logarithmic barrier method. *Geophys J Int*, 2003, 152: 251-265.

[17] Liu, G., Yan, H., Meng, X., Chen, Z. An extension of gravity probability tomography imaging. *Journal of Applied Geophysics*, 2014, 102: 62-67.

[18] MohammadRezaie, AliMoradzadeh and Ali Neja-tiKalateh, Fast 3D inversion of gravity data using solution space preconditioned lanczos bidiagonal-ization, *Journal of Applied Geophysics*, 2017, 136: 42-50.

[19] Mauriello, P., Patella, D.. Gravity probability tomog-raphy: a new tool for buried mass distribution imag-ing. *Geophysical Prospecting*, 2001, 49: 1-12.

- [20] Meng, X.H., Liu, G.F., Chen, Z.X., Guo, L.H.. 3-D gravity and magnetic inversion for physical properties based on residual anomaly correlation (in Chinese with English abstract). *Chinese Journal of Geophysics*, 2012, 55: 304-309.
- [21] Moustafa A.R.. Structural setting and tectonic evolution of North Sinai folds, Egypt. In Homberg, G. and Bachmann, M. (eds). *Evolution of the Levant Margin and Western Arabia Platform since the Mesozoic*. Geological Society, London, Special Publications, 2015, 341: 37-63.
- [22] Patella, D.. Introduction to ground surface self-potential tomography. *Geophysical Prospecting*, 1997, 45: 653-681.
- [23] Portniaguine, O., Zhdanov, M.S.. Focusing geophysical inversion images. *Geophysics*, 1999, 64: 874-887; 3-D magnetic inversion with data compression and image focusing. *Geophysics*, 2002, 67: 1532-1541.
- [24] Shamsipour, P., Chouteau, M., Marcotte, D.. 3D stochastic inversion of magnetic data. *Journal of Applied Geophysics*, 2011, 73: 336-347.
- [25] Shamsipour, P., Marcotte, D., Chouteau, M., Keating, P.. 3D stochastic inversion of gravity data using cokriging and cosimulation. *Geophysics*, 2010, 75: I1-I10.
- [26] Tikhonov, A.N., Arsenin, V.Y.. *Solution of ill-posed Problems*. Winston, 1977.
- [27] Yao, C.L.. High speed computation and efficient storage in 3D gravity and magnetic inversion based on genetic algorithms (in Chinese with English abstract). *Chinese Journal of Geophysics*, 2003, 46: 252-258.
- [28] Yao, C.L., Zheng, Y.M., Zhang, Y.W.. 3-D gravity and magnetic inversion for physical properties using stochastic subspaces (in Chinese with English abstract). *Chinese Journal of Geophysics*, 2007, 50: 1576-1583.
- [29] Zhdanov, M.S.. *Tutorial: Regularization in inversion theory*. Center for Wave Phenomena, 1993: 1-47.
- [30] Zhdanov, M.S.. *Geophysical inverse theory and regularization problems*. Elsevier, 2002.
- [31] Zhao, G.D., Chen B., Chen L.W., Liu J.X., Ren Z.Y.. High-accuracy 3D Fourier forward modeling of gravity field based on the Gauss-FFT technique. *Journal of Applied Geophysics*, 2018, 150: 294-303.